Received August 23, 2020, accepted September 3, 2020, date of publication September 7, 2020,
date of current version September 22, 2020.

Digital Object Identifier 10.1109/ACCESS.2020.3022361

Standstill Time-Domain Response Parameter Estimation of the Large Synchronous Condenser in Arbitrary Rotor Position

YIMING MA, LIBING ZHOU, AND JIN WANG, (Member, IEEE)
State Key Laboratory of Advanced Electromagnetic Engineering and Technology, School of Electrical and Electronic Engineering, Huazhong University of Science and Technology, Wuhan 430074, China

Corresponding author: Jin Wang (hustwj@126.com)

ABSTRACT The necessity to align the rotor with the d-q magnetic axes is the main obstacle for the wide application of synchronous machine standstill parameter tests, especially for the high-power units. This paper presents an arbitrary rotor position parameter estimation method for standstill time-domain response (SSTRs) tests and applied on a 300 MVar, 20 kV large synchronous condenser, a DC step voltage signal is selected as the input signal. Firstly, a frequency-domain Dalton-Cameron transformation is demonstrated and used to simultaneously obtain both axes' operational inductances in an arbitrary rotor position, thus eliminating the need for the rotor prepositioning process. Then, a novel analytical parameter estimation method combined with an I/T transformation is proposed, all the parameters of both axes are determined without extra tests, the mutual leakage flux between the field winding and the d-axis damper winding is also taken in account. To validate the proposed method, this test is carried out and its parameter estimation results are compared against that of the three-phase sudden short-circuit test and the traditional SSTR test. Estimation results are given in the form of I-type and T-type circuits, the maximum relative error no more than 6% and 10%, respectively.

INDEX TERMS Parameter estimation, large synchronous condenser, standstill time-domain response, arbitrary rotor position.

NOMENCLATURE

u_{abc}	stator three-phase voltage
u_s	stator input voltage
i_{abc}	stator three-phase current
u_d, u_q	d- and q- axis voltage, respectively
i_d, i_q	d- and q- axis current, respectively
u_f	field winding voltage
i_f, i_D	field and damper winding current, respectively
i_{Q1}, i_{Q2}	q-axis damper winding 1, 2 current, respectively
L_d, L_q	d- and q- axis synchronous inductance, respectively
L_{ad}, L_{aq}	d- and q- axis armature reaction inductance, respectively
L_{sl}	stator leakage inductance
L_{fl}, L_{dl}	field and damper winding leakage inductance, respectively
L_{Ql1}, L_{Ql2}	q-axis damper winding 1, 2 leakage inductance, respectively
L'_d, L''_d	d-axis transient and sub-transient inductance, respectively
L''_q, L'''_q	q-axis sub-transient and sub-subtransient inductance, respectively
T'_d, T''_d	d-axis transient and sub-transient short-circuit time constant, respectively
T'_{d0}, T''_{d0}	d-axis transient and sub-transient open-circuit time constant, respectively
T''_q, T'''_q	q-axis sub-transient and sub-subtransient short-circuit time constant, respectively
T''_{q0}, T'''_{q0}	q-axis sub-transient and sub-subtransient open-circuit time constant, respectively
$T_{\sigma f}$, $T_{\sigma D}$	field and damper winding leakage time constant, respectively
r_a, r_s	stator and armature resistance, respectively

The associate editor coordinating the review of this manuscript and approving it for publication was Giambattista Gruosso.

r_f, r_D	field and damper winding resistance, respectively
r_{Q1}, r_{Q2}	q-axis damper winding 1, 2 resistance, respectively
θ	rotor position angle

I. INTRODUCTION

Ultra-high voltage direct current (UHVDC) transmission projects have seen a rapid uptake in some Asian countries in recent years [1], [2]. To ensure the stable transmission of power, the converter stations of UHVDC systems need a large amount of reactive power, especially under conditions with more dynamic variation [3]. The lack of dynamic reactive power may threaten the voltage stability of AC bus in converter stations, therefore resulting in a series of serious faults, such as commutation failure, DC bipolar blocking, and so on [4]. Existing widely used reactive power compensation devices, such as static var compensation devices and static synchronous compensators, are difficult to fulfill the demand due to capacity limitations.

In recent years, large synchronous condensers (LSCs) had been suggested as the main source for dynamic reactive power compensation of UHVDC transmission systems by the relevant researchers and authorities [5]–[8]. Today, dozens of 300 MVar LSCs have been successfully installed in UHVDC projects across China. The LSC is a type of synchronous machine without mechanical load and operating in a continuous no-load condition, it can be regarded as a pure reactive power source. Unlike traditional synchronous condensers applied for steady-state reactive compensation, LSCs are more concerned with dynamic reactive compensation, thus a series of special design had been employed to obtain better dynamic reactive power compensation abilities [7], [8].

The accurate estimation of the LSC's dynamic parameters is the most important part of analyzing its reactive compensation characteristics, and it also plays a vital role in the performance evaluation and protection setting. The most commonly used synchronous machine parameter test method is the three-phase sudden short-circuit test [9]. However, a large transient current will be generated during this test, posing risks on high-power unit tests. Additionally, only d-axis equivalent circuit parameters can be obtained using this test. To tackle these drawbacks, standstill frequency response (SSFR) tests were recommended by the IEEE standard [9]. SSFR tests give a new way to identify parameters at standstill, they greatly enhance the safety of test and can identify q-axis parameters effectively. Nevertheless, this type of test is time-consuming at low frequencies and its device requirement is strict while some standstill time-domain response (SSTR) tests can offer an attractive alternative [10].

The test procedure of SSTR tests can be briefly expressed as follows: when the machine is at standstill, let the rotor aligns with the desired position for the d-axis and q-axis tests, and the parameters of the two axes model must be identified respectively. A voltage signal is injected into stator terminals and the transient current responses of armature windings and the field winding are recorded for parameter estimation [11]. In this kind of test, the type of input signal can be flexibly selected, such as DC step signal [10]–[12], DC pulse signal [13], sinc signal [14], and chirp signal [15], [16]. Their advantages lie in the safety and short duration at the experimental stage.

Similar to other standstills test methods, such as SSFR and DC decay [17], pre-positioning of the rotor is still inevitable in SSTR tests, as the method used in [11]. This alignment process is difficult for high-power units [18], especially for those without a prime mover, just like LSCs, which will require an additional prime mover or other barring devices. Furthermore, for synchronous machines with a large number of pole pairs, a small mechanical angle error during the positioning process will cause a large electrical angle error, therefore greatly reducing the accuracy of parameter estimation. To make this test method applicable, a method suitable for an arbitrary rotor position is urgently needed.

Some related works had been previously reported for other types of standstill tests. Dalton and Cameron proposed a transformation method for determining the two axes sub-transient reactances in arbitrary rotor positions [19]. Maurer summarized and proposed two arbitrary rotor position parameter identification methods for the DC decay test [18]. Oteafy gave an advanced arbitrary rotor position estimation technique where the stator windings were excited by a three-phase chirp signal, his method needed to know the rotor angle in advance [16]. However, in the existing SSTR method literature [10]–[15], the capacity of the prototypes used in their tests was relatively small, it did not involve problems such as the difficulty in rotor positioning or the lack of a matching prime mover. Thus, there was no appropriate method had been proposed that allows SSTR testing in an arbitrary rotor position.

In this paper, a SSTR test method in an arbitrary rotor position for the LSC is proposed. Combined with an I/T transformation, all parameters in the models of both axes are predicted in an analytically way with the mutual leakage inductance taken into account. Since this test was performed in a converter station, subject to test conditions, the most typical and readily available DC step voltage signal in SSTR tests was chosen as the input. It is called 'DC step voltage test' in the following. Compared with the previous works relevant to SSTR tests [10]–[15], the greatest improvement of the proposed method is that this test and its parameter identification method can be applied to arbitrary rotor position without rotor pre-positioning, so it is especially suitable for high-power units.

The rest of this paper is organized as follows: In Section II, based on the structural features of the LSC, a mathematical model considering the rotor side mutual leakage flux is established. Meanwhile, the test principles and parameter estimation process of the DC step voltage test are illustrated, including an I/T transformation of equivalent circuits. In Section III, an expanded frequency-domain

Dalton-Cameron (D-C) transformation and its detailed analytical proof process are given. Using this transformation, the parameters of both axes can be simultaneously estimated. In Section IV, the data processing method and the specific parameter estimation process are introduced. Without extra tests, all parameters of both axes can be analytically determined, including the mutual leakage inductance L_{ml} and the characteristic inductance L_c. In Section V, the proposed test method is validated by the experimental data of a 300 MVar, 20 kV, 50 Hz LSC and compared against the traditional SSTR test given in [10, 11] and the three-phase sudden short-circuit test. Section VI gives the conclusions.

II. DESCRIPTION OF MODEL AND TEST

A. MATHEMATICAL MODEL OF LSC

A schematic of the LSC as shown in Fig. 1. For the sake of clarity, the stator winding and field winding are not shown.

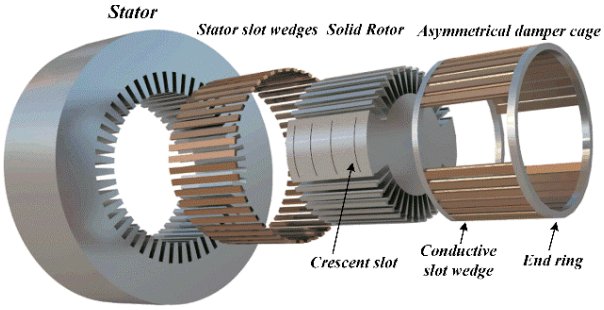

FIGURE 1. Schematic of the LSC.

According to the machine structure shown in Fig. 1, the following special design considerations have been made for LSCs to acquire better dynamic reactive power compensation characteristics [7].

(1) Non-salient pole solid rotor structure similar to that of large turbo-generators is adopted by LSCs, while the traditional synchronous condensers are always designed with salient pole laminated rotor. One pole pair structure is used to increase the speed as much as possible and to reduce the machine volume.

(2) To extend the transient process determined by the damper windings, conductive rotor slot wedges are adopted and welded with silver-plated end rings to form a damper cage with high conductivity. There are a series of crescent slots in the direction of the rotor's large tooth to balance the stiffness in the XY direction and to avoid double frequency vibration, it also affects the solid rotor's damping effect.

(3) By reducing the rotor leakage reactance while increasing the field winding resistance, the d-axis transient time constant T_d' has been significantly reduced, therefore it can respond to the excitation control faster.

The electrical dynamics of a synchronous machine is generally described by the equivalent circuits model according to the two-axis theory [10]. The most famous one is the five-winding model in which only one damper winding is considered for both axes. Nevertheless, for synchronous machines with solid rotors, the induced current and damping effect of the solid rotor during transient processes requires at least one additional rotor circuit branch to describe [20], [21].

Owing to the skin effect, the induced current in the solid rotor is mainly concentrated on the tooth top. However, thanks to the crescent slots on the large tooth surface, the induced current loops of this part are cut off, which greatly weakens the induced current. Thus, in the d-axis model, the damping effect of the solid rotor can be set aside. Besides, the damper cage formed by conductive slots wedges is located directly above the field winding, no flux only intersects with the former and do not enclose the latter, as shown in Fig. 2. This mutual leakage flux leads to a mutual leakage inductance between the damper winding and the field winding. It had been proved that the consideration of this inductance could improve the prediction of the field winding current reaching a higher accuracy [10], [21]. The transient process of LSCs involves fast response and control of the excitation system, it requires the LSC model to accurately predict the transient field current, therefore, the mutual leakage inductance should be taken into account in the d-axis model.

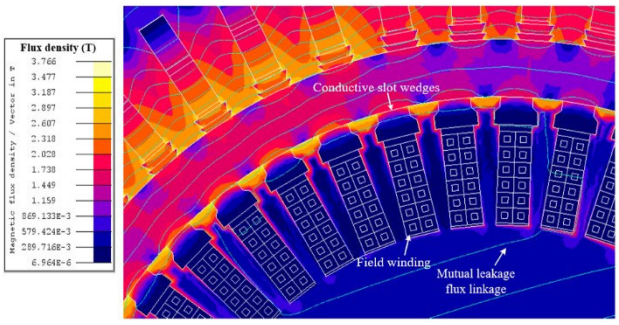

FIGURE 2. Flux distribution in a transient process.

Based on the above analysis, the following assumptions and considerations are made in determining the model for the LSC.

(1) The damping effects of the damper cage and the solid rotor are considered respectively, two parallel damping circuits are formed in the transient model.

(2) Since the induced current loops on the large tooth surface are cut off by the crescent slots, the damping circuit corresponding to the solid rotor in the d-axis model is discarded.

(3) The mutual leakage inductance between the d-axis damper winding and the field winding is taken into account for higher accuracy of the field current prediction.

The d-axis and q-axis transient mathematical model of the LSC is shown in Fig. 3.

B. DC STEP VOLTAGE TEST

The DC step voltage test consists of applying a DC step voltage signal at two stator phases with the field winding shorted while the machine rotor is stationary [10]. The test is performed after the rotor is positioned along the d-axis

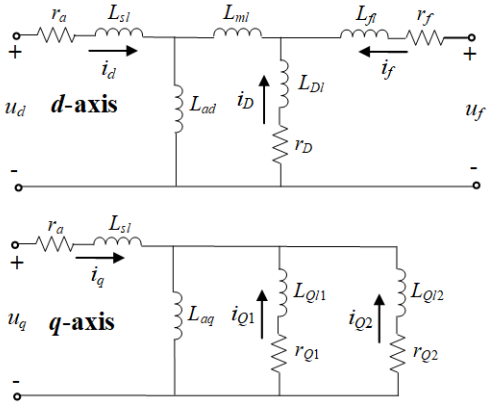

FIGURE 3. Equivalent circuits of the *d*-axis and *q*-axis.

or q-axis, so the two axes parameters must be respectively estimated. The dynamic response curves of the armature winding current and the field winding current are recorded and used for parameter estimation, a schematic of this test is shown in Fig. 4.

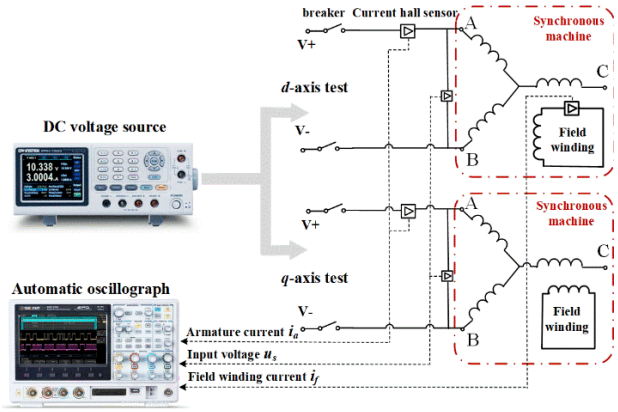

FIGURE 4. Schematic of the DC step voltage test.

Similar to SSFR tests, the two axes' operational inductances are the core of parameter estimation. Considering the number of rotor circuits is N, the operational inductances are shown as follows [11],

$$L_d(s) = L_d \frac{(1+sT'_d)(1+sT''_d)\cdots(1+sT_d^{(N+1)})}{(1+sT'_{d0})(1+sT''_{d0})\cdots(1+sT_{d0}^{(N+1)})} \quad (1)$$

$$L_q(s) = L_q \frac{(1+sT''_q)\cdots(1+sT_q^{(N+1)})}{(1+sT''_{q0})\cdots(1+sT_{q0}^{(N+1)})} \quad (2)$$

Eq. (1) and (2) are defined based on the assumption of equal mutual fluxes along the axis. However, since the mutual leakage inductance is considered, it is no longer valid. An I/T transformation can be adopted to dismiss this mutual leakage inductance in the d-axis model and transform the circuits into a parallel form [21], as shown in Fig. 5. Therefore, the operational inductance in the above form can still be used for parameters estimation. For example, the operational

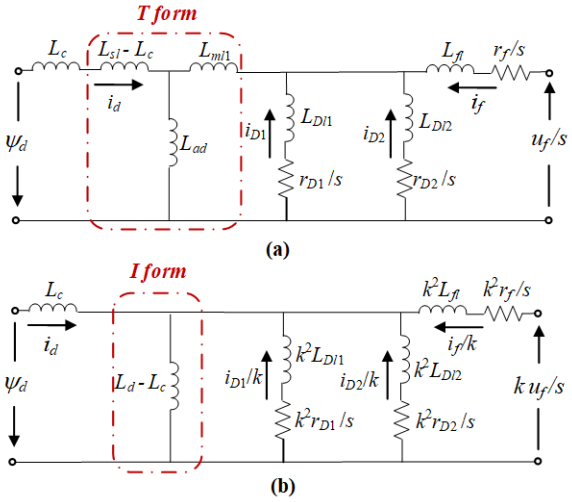

FIGURE 5. I/T transformation. (a) T-type circuit; (b) I-type circuit.

inductances of Fig. 5(b) is shown as follows. The subscript I indicates the I-type circuit.

$$L_{dI}(s) = L_d \frac{(1+sT'_{dI})(1+sT''_{dI})}{(1+sT'_{dI0})(1+sT''_{dI0})} \quad (3)$$

The I/T transformation shown in Fig. 5 satisfies [20],

$$\frac{1}{L_c - L_{sl}} = \frac{1}{L_d - L_{sl}} + \frac{1}{L_{ml}} \quad (4)$$

$$k = \frac{L_d - L_c}{L_d - L_{sl}} \quad (5)$$

Appendix I gives a more detailed introduction of the I/T transformation. The rotor side mutual leakage inductance was also considered in the literature [10], [14], [15], and the authors adopted the state space equation to numerically estimate the operational inductance. Different from them, this paper gives an analytical estimation method based on the I/T transformation.

III. TEST METHOD FOR ARBITRARY ROTOR POSITION

In the traditional DC step voltage test and other stand-still tests, the rotor pre-positioning is necessary [10]–[15], which is difficult to perform on high-power units, thus greatly reducing their applicability. In this section, a new test method in arbitrary rotor positions will be introduced so that the pre-positioning process can be omitted. To simplify the expressions of the following analytical derivation process, the traditional five-winding model based on the assumption of equal mutual fluxes is used.

A. TRANSFER FUNCTION

To analysis the relationship between the input voltage signal and the output current signal, it is first necessary to establish a transfer function between them. The condition that the rotor is in an arbitrary position, the field winding is shorted and the input voltage signal is applied to the phase A and B of

the stator winding is studied as an example. The stator phase voltage u_{abc} and phase current i_{abc} satisfy

$$\begin{cases} u_a - u_b = u_s \\ i_a = -i_b, i_c = 0 \end{cases} \tag{6}$$

Then, according to the voltage balance equations of each winding of two axes, the frequency-domain current of phase A and the input voltage signal have the following transfer function [18]. The derivation is given in Appendix 2.

$$i_a(s) = \frac{P_f(s)P_Q(s)}{P_{ab}(s)} u_s(s) \tag{7}$$

where

$$P_f(s) = (1 + sT'_{d0})(1 + sT''_{d0}) \tag{8}$$

$$P_Q(s) = 1 + sT''_{q0} \tag{9}$$

$$\begin{aligned} P_{ab}(s) = {} & 2P_f(s)P_Q(s)\left[r_s + \frac{1}{3}s(\alpha^2 L_d + \beta^2 L_q)\right] \\ & -\frac{2}{3}s^2 P_Q(s)\alpha^2 L_{ad}^2 \left(\frac{1 + sT_{\sigma D}}{r_f} + \frac{1 + sT_{\sigma f}}{r_D}\right) \\ & -\frac{2}{3}s^2 P_f(s)\frac{\beta^2 L_{aq}^2}{r_Q} \end{aligned} \tag{10}$$

$$\alpha = \cos\theta - \cos(\theta - \frac{2}{3}\pi)$$

$$\beta = \sin\theta - \sin(\theta - \frac{2}{3}\pi) \tag{11}$$

From (4), this transfer function is related to both the two axes parameters and the rotor position θ. It is mentioned in [18] that by analyzing the zeros and poles of this transfer function, the parameters are identical. However, this method relies on multiple sets of test data in different rotor positions to get the zeros and poles, the rotation of the rotor is still necessary, which has low operability for high-power units and greatly increases the required tests.

B. FREQUENCY-DOMAIN D-C TRANSFORMATION

To avoid the drawbacks of parameter estimation directly based on the transfer function, a method that is easier to implement and requires fewer tests is proposed, which is inspired by a transformation proposed by Dalton and Cameron for solving two axes sub-transient reactance [19]. While keeping the rotor in an arbitrary position and having the field winding shorted, their test is carried out by applying a single-phase, rated-frequency voltage signal to the armature windings combined two-by-two. Based on the assumption that the variation of the sub-transient reactance in one pole span satisfied a sinusoidal periodic function [19], they gave the following equations,

$$\begin{aligned} X''_d &= \frac{k + M}{2} \\ X''_q &= \frac{k - M}{2} \end{aligned} \tag{12}$$

where

$$k = \frac{X_A + X_B + X_C}{3} \tag{13}$$

$$M = \sqrt{(X_B - k)^2 + \frac{(X_C - X_A)^2}{3}} \tag{14}$$

In the above equations, X_A, X_B, and X_C denote the measured reactances; X''_d and X''_q denote the d- and q- axis sub-transient reactances, respectively. The traditional D-C transformation is only solved for the sub-transient reactances. Based on the transfer function established in Section III-A, a frequency-domain D-C transformation is proposed to realize the parameter estimation of both axes at the same time.

According to (4), when the voltage signal is applied to phase A-B, the corresponding frequency-domain impedance is,

$$\begin{aligned} Z_{ab}(s) = \frac{u_s(s)}{i_a(s)} &= \frac{P_{ab}(s)}{P_f(s)P_Q(s)} \\ &= M(s)\cos(2\theta + \frac{\pi}{3}) + k(s) \end{aligned} \tag{15}$$

where

$$\begin{aligned} M(s) = {} & [L_d s - L_{ad}^2 s^2 (\frac{1 + sT_{\sigma D}}{r_f} + \frac{1 + sT_{\sigma f}}{r_D})/P_f(s)] \\ & -[L_q s - L_{aq}^2 s^2/(r_Q \cdot P_Q(s))] \end{aligned} \tag{16}$$

$$\begin{aligned} k(s) = {} & [L_d s - L_{ad}^2 s^2 (\frac{1 + sT_{\sigma D}}{r_f} + \frac{1 + sT_{\sigma f}}{r_D})/P_f(s)] \\ & +[L_q s - L_{aq}^2 s^2/(r_Q \cdot P_Q(s))] + 2r_s \end{aligned} \tag{17}$$

When the coupling of the stator windings changes to phase B-C or phase C-A, the following impedances are yielded.

$$Z_{bc}(s) = \frac{u_s(s)}{i_b(s)} = M(s)\cos(2\theta - \pi) + k(s) \tag{18}$$

$$Z_{ca}(s) = \frac{u_s(s)}{i_c(s)} = M(s)\cos(2\theta + \frac{5\pi}{3}) + k(s) \tag{19}$$

Eq. (12), (15) and (16) correspond to Fig. 6.

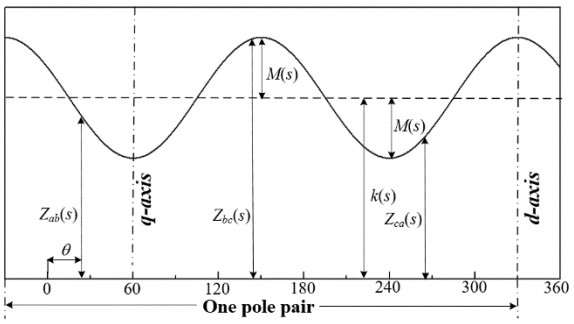

FIGURE 6. Variation curve of frequency-domain impedance.

From Fig. 6, $M(s)$ indicates the amplitude of the cosine function part while $k(s)$ indicates an offset. Thus, $k(s)$ and $M(s)$ can be calculated by

$$k(s) = \frac{Z_{ab}(s) + Z_{bc}(s) + Z_{ca}(s)}{3} \tag{20}$$

$$M(s) = \sqrt{(Z_{bc}(s) - k(s))^2 + \frac{(Z_{ca}(s) - Z_{ab}(s))^2}{3}} \tag{21}$$

For the electric excitation synchronous machines, the d-axis impedance is generally greater than that of the q-axis, therefore the frequency-domain impedance takes the maximum value at the d-axis while takes the minimum value at the q-axis [17].

$$Z_d(s) = \frac{k(s) + M(s)}{2}$$
$$Z_q(s) = \frac{k(s) - M(s)}{2} \tag{22}$$

Further, the operational inductances are obtained,

$$L_d(s) = \frac{Z_d(s) - r_s}{s}$$
$$L_q(s) = \frac{Z_q(s) - r_s}{s} \tag{23}$$

According to the forms of both axes operational inductances, by comparing (1) and (2) with (23), one can easily get the synchronous inductances and the transient time constants of both axes. Further, other transient inductances can also be calculated analytically.

In the above derivation, (20) and (21) are regarded as the frequency-domain extensions of (13) and (14). However, to perform this transformation, the resistance r_s should maintain the same when the voltage signals are input to different stator ports. In fact, besides the stator winding resistance, r_s also includes the resistances by the external test equipment and the contact resistances, which is difficult to maintain the same in each test. To circumvent this problem, the above transformation needs a modification.

From (14), the item related to r_s is independent, therefore it can be eliminated before the transformation. For example,

$$Z'_{ab}(s) = Z_{ab}(s) - 2r_{sab} \tag{24}$$

where r_{sab} denotes the phase resistance when the coupling of the stator winding is phase A-B. For a DC step voltage test, the value of armature resistance r_s can be easily calculated by the ratio of the step voltage value to the steady-state current value. In the same way, $Z'_{bc}(s)$ and $Z'_{\mathrm{ca}}(s)$ are obtained. Then, three impedances are substituted into (20) and (21) so that $k'(s)$ and $M'(s)$ are available.

Finally, the operational inductances are as follows

$$L_d(s) = \frac{k'(s) + M'(s)}{2s}$$
$$L_q(s) = \frac{k'(s) - M'(s)}{2s} \tag{25}$$

Besides, using this method, not only the operational inductance of both axes can be simultaneously estimated, but also the rotor position angle θ is available.

$$\theta = \frac{1}{2}\mathrm{arc\,cot}\left[\frac{\sqrt{3}(Z_{ab}(s) - k(s))}{Z_{ca}(s) - Z_{bc}(s)}\right] - \frac{\pi}{6}$$
$$= \frac{1}{2}\mathrm{arc\,cot}\left[\frac{\sqrt{3}(Z'_{ab}(s) - k'(s))}{Z'_{ca}(s) - Z'_{bc}(s)}\right] - \frac{\pi}{6} \tag{26}$$

C. FREQUENCY-DOMAIN D-C TRANSFORMATION

The transformation established in Section III-B depends on the following test to obtain the parameters of both axes in an arbitrary rotor position.

· **Step 1:** Keeping the rotor in an arbitrary position and having the field winding short-circuited.

· **Step 2:** The DC step voltage signal is applied to the stator terminal under different stator winding couplings.

· **Step 3:** The transient armature current responses and field winding responses of each test should be recorded.

· **Step 4:** Three armature current responses are curve-fitted to calculate the operational inductances of both axes. Then, other parameters of interest are assessed.

Three different stator winding couplings and their connection with the signal source are given in Table 1.

TABLE 1. Different Couplings of Stator Winding.

	Phase A	Phase B	Phase C
Coupling I	▲	▼	○
Coupling II	○	▲	▼
Coupling III	▼	○	▲

▲: Connected to the positive end ▼: Connected to the negative end ○: Empty

IV. PARAMETER ESTIMATION

The premise of using the above frequency-domain D-C transformation is to accurately obtain the frequency-domain expressions of the armature current responses, namely $I_{ab}(s)$, $I_{bc}(s)$, and $I_{ca}(s)$, so that the time-domain curve fitting of current responses is a key issue. The processing of the current responses mainly includes the following two aspects.

A. CURRENT RESPONSES DE-NOISING

Since a small DC-step signal is applied to the stator winding during the test, there is a large amount of noise in the recorded armature current responses, the de-nosing of the recorded response curves is necessary so that the error during the numerical fitting process can be reduced. A well-known wavelet threshold de-noising algorithm is adopted [22]. In this algorithm, an improved compromise for soft/hard thresholds method is used to overcome the drawbacks of the hard thresholds and soft thresholds. The selected threshold function is as follows

$$\hat{w} = \begin{cases} sgn(w) \cdot (|w| - \dfrac{b\lambda}{a^{||w|-\lambda|} + b - 1}) & |w| \geq \lambda \\ 0 & |w| < \lambda \end{cases} \tag{27}$$

where a and b are adjustable coefficients that greater than 1; λ denotes the threshold. It can be proved that when a approaches 1, this function is similar to the soft threshold function; when a approaches positive infinity, it is similar to the hard threshold function. This threshold is asymptote with $y = x$, which can reduce the deviation between the estimated wavelet coefficient and the actual one.

The above algorithm is coded in python with the assist of the Pywavelet toolkit package. After testing the denoising effect of ten wavelet sets from db1 to db10, the best de-noising effect is obtained by using the db3 wavelet with four layers when a is set to 4000 and b is 13.5. The de-noised curve is shown in the next section.

B. CURVE FITTING

For the current responses of the armature winding, assuming only one damper winding is considered for both axes, $P_{ab}(s)$ can be rewritten as the following polynomial form. The coefficients of this polynomial are given in Appendix II.

$$P_{ab}(s) = \lambda_4(\theta)s^4 + \lambda_3(\theta)s^3 + \lambda_2(\theta)s^2 + \lambda_1(\theta)s + \lambda_0(\theta) \quad (28)$$

From (27), the highest power of $P_{ab}(s)$ is 4, which corresponds to four non-zero roots. Since a DC step voltage signal is input, there are four attenuation components and one steady-state component in the transient armature current. Now, if more damper windings are considered, like the model of LSC, one additional attenuation component should be added, thus yielding the following time-domain general solution.

$$\hat{i}_s(t) = \alpha_1 e^{-\beta_1 t} + \alpha_2 e^{-\beta_2 t} + \alpha_3 e^{-\beta_3 t} + \alpha_4 e^{-\beta_4 t} + \alpha_5 e^{-\beta_5 t} + i_\infty \quad (29)$$

where a_1 to a_5 and b_1 to b_5 denote the amplitude coefficients and attenuation coefficients of the attenuation components, respectively; i_s denotes the armature current while i_∞ is its steady-state value that can be directly determined by the recorded current waves.

The curve fitting of the field winding induced current responses is also required to facilitate the availability of the T-type circuit parameters. Under coupling I, according to Fig. 5(b), the relationship between the field current and the armature current can be established, so the time-domain general solution of the field current is

$$\frac{i_{f(A-B)}(s)}{k} = -\frac{2\alpha(L_d - L_c)}{3k^2 r_f} \frac{s(1+sT_{\sigma DI})}{(1+sT'_{dI0})(1+sT''_{dI0})} i_a(s) \quad (30)$$

Define the transfer between the armature current $i_a(s)$ and $i_{f(A-B)}$ (s) as $G_f(s)$,

$$G_f(s) = -\frac{2\alpha(L_d - L_c)(1+sT_{\sigma DI})}{3kr_f} \quad (31)$$

Then, i_f can be expressed in a more common form and its time-domain general solution is yielded.

$$i_{f(A-B)}(s) = \frac{sG_f(s)}{(1+sT'_{dI0})(1+sT''_{dI0})} i_a(s) \quad (32)$$

$$\hat{i}_f(t) = \gamma_1 e^{-\eta_1 t} + \gamma_2 e^{-\eta_2 t} + \gamma_3 e^{-\eta_3 t} + \gamma_4 e^{-\eta_4 t} + \gamma_5 e^{-\eta_5 t} \quad (33)$$

where γ_1 to γ_5 and η_1 to η_5 denote the amplitude coefficients and attenuation coefficients of the attenuation components, respectively. The coefficients in (29) and (33) are determined by the minimization of the following cost functions.

$$\min J_s = \frac{1}{2}\sum_{i=1}^{N_s} [(i_s(t_i) - i_\infty) - \hat{i}_s(t_i)]^2 \quad (34)$$

$$\min J_f = \frac{1}{2}\sum_{i=1}^{N_f} [i_f(t_i) - \hat{i}_f(t_i)]^2 \quad (35)$$

where $i_s(t)$ and $i_f(t)$ denote the measured value of transient current responses at time t; N_s and N_f denote the number of measurement points.

To accomplish the minimization of the cost functions, a series of heuristic algorithms were used in related works so that the initial values dependence problem of the traditional curve fitting algorithm, like the Levenberg-Marquardt algorithm, can be mitigated [10], [14]. In this work, a simulated annealing particle swarm optimization (SAPSO) algorithm is adopted to deal with this issue. The reference values of the PSO's hyper-parameters are set as: the max generation is 300; the number of pop size is 50; the personal and social acceleration coefficients are 1.9 and 1.7, respectively. An adaptive temperature attenuation factor is used for the SA algorithm [7], which can be expressed as,

$$\alpha = \lambda + [1 - \exp(f_i - f_{avg})] \cdot N(0,1)/T_k \quad (36)$$

where α is the current attenuation factor; λ is the initial attenuation factor and set as 0.99; f_i is the individual particle fitness; f_{avg} denotes the population average fitness; N (0,1) is a Gaussian random number with variance 1 and mean 0; T_k is the temperature in the previous iteration.

C. T-TYPE CIRCUIT PARAMETER ESTIMATION

Using the curve fitting results of the armature currents and the frequency-domain D-C transformation, the operational inductance $L_d(s)$ and $L_q(s)$ can be calculated. Nevertheless, taking the d-axis for example, in this way, only five independent parameters are obtained, including the d-axis synchronous inductance L_d, two short-circuit time constants T'_d, T''_d and two open-circuit time constants T'_{d0}, T''_{d0}.

To identify the seven unknown parameters of the T-type circuit (Fig. 5(a)), the five independent parameters obtained from the armature current are not sufficient. Therefore, it is necessary to use the transfer relationship between the field current i_f and the armature current i_a to introduce new independent items so that all the parameters of the T-type circuit can be fully determined. The specific steps are:

· **Step 1:** The armature current and field current under one stator winding coupling is selected and curve-fitted using SAPSO in the time-domain. Then, converted them into a rational fraction form in the frequency-domain. Here, i_a and $i_{f(A-B)}$ are selected.

· **Step 2:** By directly analyzing the zeros of $i_{f(A-B)}(s)$ and $i_a(s)$, the leakage time constant $T_{\sigma DI}$ can be obtained.

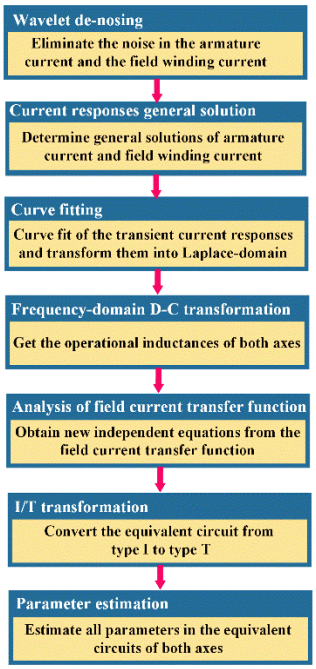

FIGURE 7. Parameter estimation flowchart.

· **Step 3:** Using $T_{\sigma DI}$, the I-type circuit with six unknown parameters is now determinable. Particularly, the items L_d-L_c and $k^2 r_f$ are obtained.

· **Step 4:** According to the armature current data of the three tests, the rotor position angle θ is calculated using (26). Then, the coefficient α is gotten using (11).

· **Step 5:** From the ratio of the coefficients of the components with the same attenuation coefficient in $i_s(t)$ and i_f(t), combined with the values of L_d-L_c, $k^2 r_f$, and α, the coefficient k is determinable.

After the above steps, two new independent parameters of k and L_c are obtained, where k represents the ratio of the change in the field winding current after considering the mutual leakage inductance, and L_c is the 'characteristic inductance', which generally measured by some specialized and complex tests, such as the method given in [21]. Now, the T-type circuit parameters can be fully determined. By the way, only one of the field current response needs a curve fitting to assist with the identification of the T-type circuit.

The flowchart corresponding to the entire parameter estimation process is as follows.

V. EXPERIMENTAL RESULTS

To validate the accuracy and rationality of the proposed test method, both the traditional DC step voltage test (described in [10], [11]) and the proposed test were performed in Guquan UHVDC converter station. The experimental site is shown in Fig. 8.

The DC step voltage signal used in these tests is generated by a battery with an air switch, the voltage waveform is shown in Fig. 9.

FIGURE 8. Experimental site.

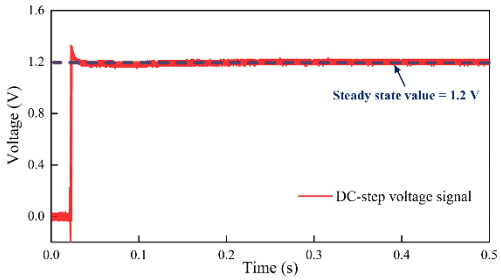

FIGURE 9. DC step voltage signal.

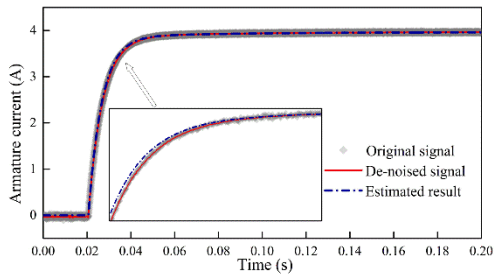

FIGURE 10. Armature current response of the *d*-axis test.

A. TRADITIONAL DC STEP VOLTAGE TEST

Since a small DC-step signal is applied to the stator winding during the test, there is a large amount of noise in the recorded armature current responses, the de-nosing of the recorded response curves is necessary so that the error during the numerical fitting process can be reduced. A well-known wavelet threshold de-noising algorithm is adopted [22]. In this algorithm, an improved compromise for soft/hard thresholds method is used to overcome the drawbacks of the hard thresholds and soft thresholds. The selected threshold function is as follows

The test is performed under coupling I and the rotor is first pre-positioned with an additional barring device using the method given in [8]. For the d-axis test, the rotor position angle θ is $-30°$ with that of the q-axis test is $60°$. The voltages and currents of both axes have the following relationship with that of the stator side,

$$\begin{cases} u_d = u_s/\sqrt{3} \\ i_d = 2i_s/\sqrt{3} \end{cases} \tag{37}$$

where the subscripts d, q, and s indicate the d-axis, the q-axis, and the stator, respectively. Taking the d-axis test as an example, the processing results of its armature current and field current response are shown in Fig. 10 and Fig. 11. During curve fitting, the time-domain expressions of both currents contain three attenuation components.

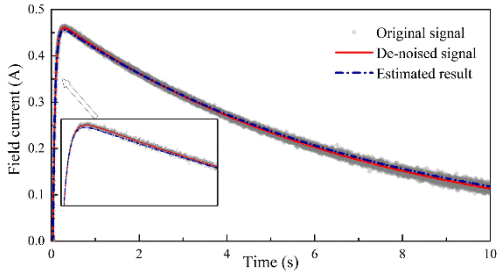

FIGURE 11. Field current response of the *d*-axis test.

After that, the d-axis operational inductance can be obtained in an analytical way similar to that of [11]. Transient inductances are calculated by

$$L'_d = L_d / \left[1 - \frac{(T'_d - T'_{d0})(T'_d - T''_{d0})}{T'_d(T'_d - T''_d)}\right] \tag{38}$$

$$L''_d = L_d \frac{T'_d T''_d}{T'_{d0} T''_{d0}} \tag{39}$$

The q-axis parameters can be similarly calculated and the parameter calculation results of both axes are given in Section V-B together with that of the proposed test.

B. TEST IN ARBITRARY ROTOR POSITION

This test is carried out in an arbitrary rotor position while the rotor pre-position is unnecessary. According to the test scheme of Section III-C, the de-noising and curve-fitting results of the armature current responses obtained by three different stator winding couplings are shown in Fig. 12. The current transient process start time is taken as time zero to facilitate comparison. After the armature current is completely stabilized, the measured current steady-state value is around 4.0A, thus the per phase armature resistance r_s of each test can be obtained. The field current response corresponding to Coupling I is selected to assist in determining the T-type circuit parameters, as Fig. 13.

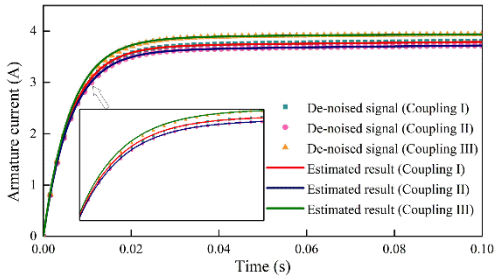

FIGURE 12. Armature currents fitting results in an arbitrary rotor position.

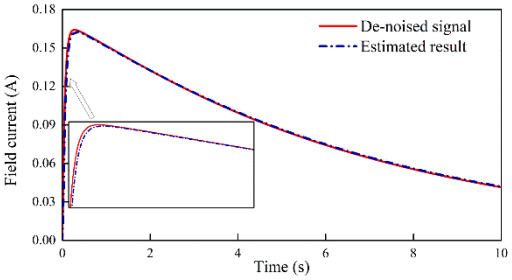

FIGURE 13. Field current (Coupling I) fitting results in an arbitrary rotor position.

TABLE 2. Time-domain Curve Fitting Data.

Item	Coupling I	Coupling II	Coupling III	Item	Field current (Coupling I)
α_1	-3.646	-3.562	-3.783	γ_1	0.0101
α_2	-0.0636	-0.0071	-0.1572	γ_2	-0.1707
α_3	-0.1145	-0.1717	-0.0144	γ_3	-0.0094
α_4	-0.1614	-0.2570	-0.0094	γ_4	-0.0086
α_5	-0.0179	-0.0051	-0.0391	γ_5	0.1786
β_1	-187.90	-188.76	-186.18	η_1	-187.90
β_2	-20.45	-20.74	-20.04	η_2	-20.45
β_3	-9.910	-9.750	-10.16	η_3	-9.910
β_4	-1.182	-1.153	-1.228	η_4	-1.182
β_5	-0.146	-0.146	-0.145	η_5	-0.146

Table 2 gives the curve fitting results.

Using the curve fitting results and the frequency-domain D-C transformation, the operational inductance of both axes are available. Further, following the steps given in Section VI-C, all parameters in the T-type circuits can be determined.

C. RESULTS AND COMPARISON

A three-phase sudden short-circuit test was also carried out to verify the proposed method. This test was performed under the condition of reducing the terminal voltage to ensure that the unsaturated parameter values were obtained. It must be pointed out that the three-phase sudden short-circuit test can only obtain the parameter values of the d-axis equivalent circuit. The test site and the short-circuit currents waveforms are shown in Fig. 14.

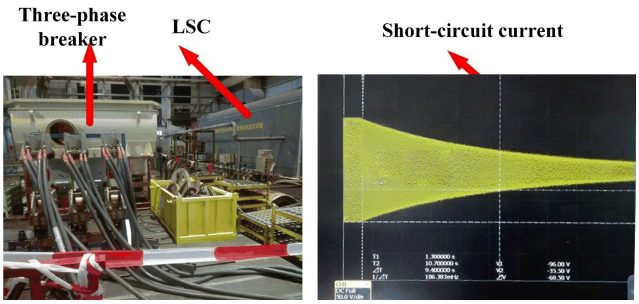

FIGURE 14. Three-phase sudden short-circuit test.

TABLE 3. Parameter Estimation Results of Three Methods.

Parameters	Proposed method	Traditional method	Short-circuit test	Error (%)
L_d	1.531 pu	1.549 pu	1.54	1.16, 0.58
$L_{dI}^{'}$	0.155 pu	0.156 pu	0.153	0.64, 1.28
$L_{dI}^{''}$	0.115 pu	0.110 pu	0.113	4.54, 1.77
L_q	1.465 pu	1.482 pu		1.15
$L_{qI}^{''}$	0.485 pu	0.514 pu		5.64
$L_{qI}^{'''}$	0.121 pu	0.123 pu		1.63
$T_{dI0}^{'}$	6.832 s	7.081 s	7.21	3.52, 5.24
$T_{dI0}^{''}$	0.0481 s	0.0497 s	0.049	3.21, 1.84
$T_{qI0}^{''}$	0.812 s	0.774 s		4.91
$T_{qI0}^{'''}$	0.0981 s	0.102 s		3.82
$T_{dI}^{'}$	0.681 s	0.701 s	0.71	2.85, 4.08
$T_{dI}^{''}$	0.0363 s	0.0358 s	0.036	1.40, 0.83
$T_{qI}^{''}$	0.177 s	0.167 s		5.98
$T_{qI}^{'''}$	0.0374 s	0.0393 s		4.83
L_c	0.113 pu	0.108 pu		4.63
θ_{estimate}	18.2°	-30°, 60°		
θ_{measure}	20°	-30°, 60°		

TABLE 4. Parameter Estimation Results of Three Methods.

Parameters	Proposed method	Traditional method	Error (%)
k	0.979	0.982	0.33
L_{ad}	1.448 pu	1.467 pu	1.29
L_{sl}	0.0831 pu	0.0817 pu	1.71
L_{ml}	0.0304 pu	0.0278 pu	9.35
L_{Dl}	0.0023 pu	0.0022 pu	4.54
L_{fl}	0.0428 pu	0.0475 pu	9.88
r_D	0.0030 pu	0.0031 pu	3.22
$r_{f,\text{estimated}}$	0.214 Ω	0.209 Ω	2.39
$r_{f,\text{measured}}$	0.195 Ω	0.195 Ω	

Table 3 shows the estimation results of two axes operational inductances and other transient inductances using the traditional test method and the proposed method. The d-axis dynamic parameters predicted by the three-phase sudden short-circuit test are also given. The characteristic inductance L_c is determined by (30). The last column of Table 3 represents the error between the results of the proposed method and that of the traditional method and short-circuit test, respectively. Meanwhile, the inductance parameters are converted to the standard value. The stator impedance base value Z_B is 2.3Ω and the field winding impedance base value Z_{fB} is 302.5Ω.

Comparison results in Table 3 prove the validity of the proposed method, the maximum error is around 5%. Then, using the steps described in Section IV-C, the coefficient k and all parameters in the T-type circuit are available, as shown in Table 4. In this way, the stator leakage inductance L_{sl} is obtained, therefore, the q-axis circuit is determinable.

From Table 4, the results of the proposed method are well-matched with that of the traditional ones, the maximum error does not exceed 10%. Since the value of k directly reflects the shunt effect of the mutual leakage reactance on the field circuit, a small change in k will have a significant impact on L_{ml} and L_{fl}, so their errors are larger.

In addition to the error caused by the non-ideal step voltage signal and the curve fitting process, the resistances also affect the accuracy of parameter estimation. For example, although the variation of the stator resistance does not theoretically affect the parameter estimation results, its value should not be too large to ensure an obvious current rise process, thereby improving the curve fitting accuracy.

According to the LSC's structure, the cross-sectional area of the equivalent damper winding is larger than that of the field winding, so the coupling between the field winding and the damper winding is stronger than the coupling between the field winding and the stator winding. Thus, a positive mutual leakage inductance L_{ml} is generated and this part of the leakage fluxes is closed by the rotor tooth, as shown in Fig. 2. Meanwhile, k is smaller than 1, therefore if L_{ml} is neglected, the field current value calculated by the model will be greater than the measured value.

D. DISCUSSION

Compared with traditional SSTR methods, the innovation of the proposed method lies in the following two aspects:

- *Test method*: A SSTR test method in arbitrary rotor position is proposed, it overcome the drawback that traditional SSTR tests require rotor pre-positioning [10]–[15], which makes it very suitable for high-capacity units.
- *Parameter identification method*: An analytical parameter identification method that can consider the rotor-side mutual leakage inductance is provided, all parameters of both axes can be simultaneously estimated without performing extra tests, rather than being measured separately as in [10]–[15].

Meanwhile, using the I/T transformation, two sets of the parameters are given in the I-type and the T-type, respectively. When only concerned with the transient response on the stator side, the former is enough; but when the field current response needs to be accurately considered, the latter offers a better alternative.

VI. CONCLUSION

To address the difficulty of rotor positioning when performing the SSTR test in high-capacity units, this paper proposes a novel SSTR test in an arbitrary rotor position with a DC step voltage signal used as the input, this test has been applied on a 300 MVar LSC. Meanwhile, combined with an I/T transformation and a frequency D-C transformation, all parameters in the equivalent circuits of both axes are simultaneously determined analytically without extra tests, in which the rotor-side mutual leakage inductance is taken into account.

The results of the proposed method are compared against that of the traditional DC step voltage test and the three-phase sudden short-circuit test. Two sets of parameters are given

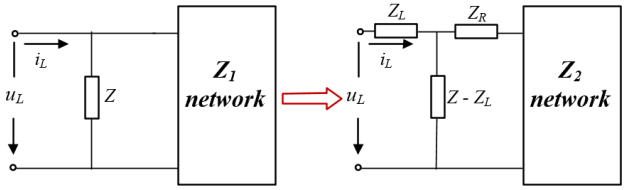

FIGURE 15. Schematic of the I/T transformation.

TABLE 5. Relations in I/T Transformation.

Item	Relation
Impedance factor	$k = Z / (Z - Z_L)$
Series impedance	$Z_R = - Z_L * k$
New elements of Z_2 network	$Z_2 = Z_1 * k^2$
Currents in Z_2 network	$I_2 = I_1 / k$
Voltages in Z_2 network	$U_2 = U_1 * k$

in the I-type circuit and T-type circuit, respectively. The maximum error in parameter estimation is about 5% for the I-type circuit and no more than 10% for the T-type circuit. Comparison results validate the rationality and accuracy of the proposed test method. The proposed method can obtain unsaturated dynamic parameters of two axes and are suitable for SSTR tests using other types of input signals. Using such methods to obtain the saturation value of dynamic parameters is one direction of future work.

APPENDIX I

The I/T transformation is a network change on the circuit, as shown in Fig. 15.

Keeping the voltage and current on the left side of Z unchanged while maintaining the power of the components on its the right side remains the same, this transformation is carried out and satisfied the relations in Table 5.

For the d-axis model in Fig. 5, letting the d-axis flux linkages and the armature current remain the same during this transformation, for the outside, these two circuits are completely equivalent [21], therefore, the circuit of Fig. 5(a) can be replaced by that of Fig. 5(b).

APPENDIX II

A detailed derivation of the transfer function in Section III-A is given in this appendix, which is based on the L_{ad} base value system and the traditional five-winding model. Similar derivations can be made when a more complex model is used. For ease of expression, during this derivation, it is assumed that the input voltage signal is applied to phase A and B.

Firstly, according to the Park equation of the stator currents, the d-axis field winding and damper winding satisfy the following equations,

$$0 = r_f i_f + \frac{2}{3}L_{ad}\cos\theta\frac{di_a}{dt} + \frac{2}{3}L_{ad}\cos(\theta - \frac{2}{3}\pi)\frac{di_b}{dt} + \frac{2}{3}L_{ad}\cos(\theta + \frac{2}{3}\pi)\frac{di_c}{dt} + L_{ad}\frac{di_D}{dt} + L_f\frac{di_f}{dt} \quad \text{(A1)}$$

$$0 = r_D i_D + \frac{2}{3}L_{ad}\cos\theta\frac{di_a}{dt} + \frac{2}{3}L_{ad}\cos(\theta - \frac{2}{3}\pi)\frac{di_b}{dt} + \frac{2}{3}L_{ad}\cos(\theta + \frac{2}{3}\pi)\frac{di_c}{dt} + L_D\frac{di_D}{dt} + L_{ad}\frac{di_f}{dt} \quad \text{(A2)}$$

Considering $i_a = -i_b$ and $i_c = 0$, the above equations are transformed into the frequency-domain. The field winding current $i_f(s)$ and the d-axis damper winding current $i_D(s)$ in the frequency-domain are represented by $i_a(s)$

$$i_f(s) = -\frac{2\alpha L_{ad}s(1 + sT_{\sigma D})}{3r_f(1 + sT'_{d0})(1 + sT''_{d0})}i_a(s) \quad \text{(A3)}$$

$$i_D(s) = -\frac{2\alpha L_{ad}s(1 + sT_{\sigma f})}{3r_D(1 + sT'_{d0})(1 + sT''_{d0})}i_a(s) \quad \text{(A4)}$$

Similarly, the voltage balance equation for the q-axis damper winding Q is as follows,

$$0 = r_D i_D - \frac{2}{3}L_{aq}\sin\theta\frac{di_a}{dt} - \frac{2}{3}L_{aq}\sin(\theta - \frac{2}{3}\pi)\frac{di_b}{dt} + L_Q\frac{di_Q}{dt} \quad \text{(A5)}$$

Transforming the time derivatives into the Laplace domain,

$$i_Q(s) = s\frac{2\beta L_{aq}i_a(s)}{3r_Q(1 + sT''_{q0})} \quad \text{(A6)}$$

Then, the stator phase voltage can be represented by the current of each winding and the inductances. For phase A,

$$u_a = r_s i_a + \frac{2}{3}(L_d\cos^2\theta + L_q\sin^2\theta + \frac{L_0}{2})\frac{di_a}{dt} + \frac{2}{3}(L_d\cos\theta\cos(\theta - \frac{2}{3}\pi) + L_q\sin\theta\sin(\theta - \frac{2}{3}\pi) + \frac{L_0}{2})\frac{di_b}{dt} + L_{ad}\cos\theta\frac{di_f}{dt} + L_{ad}\cos\theta\frac{di_D}{dt} - L_{aq}\sin\theta\frac{di_Q}{dt} \quad \text{(A7)}$$

For the voltage of phase B,

$$u_b = \frac{2}{3}(L_d\cos\theta\cos(\theta - \frac{2}{3}\pi) + L_q\sin\theta\sin(\theta - \frac{2}{3}\pi) + \frac{L_0}{2})\frac{di_a}{dt} + \frac{2}{3}(L_d\cos^2(\theta - \frac{2}{3}\pi) + L_q\sin^2(\theta - \frac{2}{3}\pi) + \frac{L_0}{2})\frac{di_b}{dt} + L_{ad}\cos(\theta - \frac{2}{3}\pi)\frac{di_f}{dt} + L_{ad}\cos(\theta - \frac{2}{3}\pi)\frac{di_D}{dt} - L_{aq}\sin(\theta - \frac{2}{3}\pi)\frac{di_Q}{dt} + r_s i_b \quad \text{(A8)}$$

Since the input voltage $u_s = u_a - u_b$, u_{ab} can be expressed as follows:

$$u_{ab} = 2r_s i_a + \frac{2}{3}(L_d\alpha\cos\theta + L_q\beta\sin\theta)\frac{di_a}{dt} + L_{ad}\cos\theta\frac{di_f}{dt} + L_{ad}\cos\theta\frac{di_D}{dt} - L_{aq}\sin\theta\frac{di_Q}{dt} - \frac{2}{3}(L_d\alpha\cos(\theta - \frac{2}{3}\pi) + L_q\beta\sin(\theta - \frac{2}{3}\pi))\frac{di_a}{dt} - L_{ad}\cos(\theta - \frac{2}{3}\pi)\frac{di_f}{dt} - L_{ad}\cos(\theta - \frac{2}{3}\pi)\frac{di_D}{dt} + L_{aq}\sin(\theta - \frac{2}{3}\pi)\frac{di_Q}{dt} \quad \text{(A9)}$$

Transforming again the above equation into the frequency-domain

$$\begin{aligned} u_{ab}(s) &= 2r_s i_a(s) + \frac{2}{3}s(\alpha^2 L_d + \beta^2 L_q) i_a(s) \\ &\quad -\frac{2}{3}\alpha^2 L_{ad}^2 s^2 \frac{1+sT_{\sigma f}}{r_D P_f(s)} i_a(s) \\ &\quad -\frac{2}{3}\alpha^2 L_{ad}^2 s^2 \frac{1+sT_{\sigma D}}{r_f P_f(s)} i_a(s) - \frac{2}{3}\beta^2 L_{aq}^2 s^2 \frac{i_a(s)}{r_Q P_Q(s)} \\ &= \frac{P_{ab}(s)}{P_f(s) P_Q(s)} i_a(s) \end{aligned} \tag{A10}$$

Furthermore, one can obtain the (7) in Section III-A and $P_{ab}(s)$ can be rewritten as the following [18],

$$\begin{aligned} P_{ab}(s) = \lambda_4(\theta)s^4 + \lambda_3(\theta)s^3 + \lambda_2(\theta)s^2 \\ +\lambda_1(\theta)s + \lambda_0(\theta) \end{aligned} \tag{A11}$$

where

$$\begin{aligned} \lambda_4(\theta) &= \frac{2}{3}(\alpha^2 L_d + \beta^2 L_q) T'_{d0} T''_{d0} T''_{q0} \\ &\quad -\frac{2}{3r_Q}\beta^2 L_{aq}^2 T'_{d0} T''_{d0} - \frac{2}{3}\alpha^2 L_{ad}^2 T''_{q0}\left(\frac{T_{\sigma D}}{r_f} + \frac{T_{\sigma f}}{r_D}\right) \end{aligned} \tag{A12}$$

$$\begin{aligned} \lambda_3(\theta) &= 2r_s T'_{d0} T''_{d0} T''_{q0} + \frac{2}{3}(\alpha^2 L_d + \beta^2 L_q) \\ &\quad \times (T'_{d0} T''_{d0} + T'_{d0} T''_{q0} + T''_{d0} T''_{q0}) \\ &\quad -\frac{2}{3r_Q}\beta^2 L_{aq}^2 (T'_{d0} + T''_{d0}) \\ &\quad -\frac{2}{3}\alpha^2 L_{ad}^2 \left(\frac{T''_{q0} + T_{\sigma D}}{r_f} + \frac{T''_{q0} + T_{\sigma f}}{r_D}\right) \end{aligned} \tag{A13}$$

$$\begin{aligned} \lambda_2(\theta) &= 2r_s(T'_{d0} T''_{d0} + T'_{d0} T''_{q0} + T''_{d0} T''_{q0}) \\ &\quad +\frac{2}{3}(\alpha^2 L_d + \beta^2 L_q)(T'_{d0} + T''_{d0} + T''_{q0}) \\ &\quad -\frac{2}{3r_Q}\beta^2 L_{aq}^2 - \frac{2}{3}\alpha^2 L_{ad}^2 \left(\frac{1}{r_f} + \frac{1}{r_D}\right) \end{aligned} \tag{A14}$$

$$\lambda_1(\theta) = 2r_s(T'_{d0} + T''_{d0} + T''_{q0}) + \frac{2}{3}(\alpha^2 L_d + \beta^2 L_q) \tag{A15}$$

$$\lambda_0(\theta) = 2r_s \tag{A16}$$

ACKNOWLEDGMENT

The authors would like to thank the help given by the staff of State Grid Hubei Electric Power Research Institute and Technology on the experiment and L. Y. Liu's kindly assistance on the proofreading of manuscripts.

REFERENCES

[1] Y. Tang, F. Li, Q. Wang, B. Chen, Y.-L. Jiang, and X.-J. Guo, "Power stability analysis of UHVDC systems hierarchically connected to AC systems," *Electr. Power Syst. Res.*, vol. 163, pp. 715–724, Oct. 2018.

[2] J. Shen, C. Cheng, X. Cheng, and J. R. Lund, "Coordinated operations of large-scale UHVDC hydropower and conventional hydro energies about regional power grid," *Energy*, vol. 95, pp. 433–446, Jan. 2016.

[3] Y. Wang, Z. Yu, Y. Mou, Y. Ji, J. Hu, S. Chen, and J. He, "Analysis and mitigation of low-frequency resonance in a long-distance UHVDC ±1100 kV system," *Electr. Power Syst. Res.*, vol. 162, pp. 118–124, Sep. 2018.

[4] H. Liu, T. Chen, Q. Sun, M. Han, Q. Li, and W. H. Siew, "Characteristics of very fast transient currents in ultra high-voltage power system with hybrid reactive power compensation," *Int. J. Electr. Power Energy Syst.*, vol. 103, pp. 587–592, Dec. 2018.

[5] P. Ying, Z. Qidi, L. Xuan, H. Yiping, and X. Guorui, "Influence of synchronous condenser on voltage stability of HVDC," in *Proc. IEEE Power Energy Soc. Gen. Meeting (PESGM)*, Aug. 2018, pp. 1–5.

[6] Y. Ma, L. Ruan, Y. Xiao, L. Zhou, J. Wang, and Q. Tao, "Modelling and analysis of the UHVDC transmission receiving system considering 300 Mvar novel synchronous condenser," *J. Eng.*, vol. 2019, no. 16, pp. 955–960, Mar. 2019.

[7] Y. Ma, Z. Ling, W. Cai, Y. Cui, L. Zhou, and J. Wang, "A novel coast-down no-load characteristic test and curve conversion method for large-scale synchronous condenser," *Electr. Power Syst. Res.*, vol. 172, pp. 77–85, Jul. 2019.

[8] P. Wang, X. Liu, Q. Mou, W. Gu, and X. Zhao, "Start-up control and grid integration characteristics of 300 MVar synchronous condenser with voltage sourced converter-based SFC," *IEEE Access*, vol. 7, pp. 176921–176934, 2019.

[9] *Test Procedures for Synchronous Machines*, IEEE Standard 115, 1995.

[10] M. A. Arjona, C. Hernandez, M. Cisneros-Gonzalez, and R. Escarela-Perez, "Estimation of synchronous generator parameters using the stand-still step-voltage test and a hybrid genetic algorithm," *Int. J. Electr. Power Energy Syst.*, vol. 35, no. 1, pp. 105–111, Feb. 2012.

[11] F. S. Sellschopp and M. A. Arjona, "Semi-analytical method for determining d -axis synchronous generator parameters using the DC step voltage test," *IET Electr. Power Appl.*, vol. 1, no. 3, pp. 348–354, 2007.

[12] A. Tumageanian and A. Keyhani, "Identification of synchronous machine linear parameters from standstill step voltage input data," *IEEE Trans. Energy Convers.*, vol. 10, no. 2, pp. 232–240, Jun. 1995.

[13] O. Mäkelä, A. Repo, and A. Arkkio, "Numerical pulse test for synchronous machines," *COMPEL Int. J. Comput. Math. Electr. Electron. Eng.*, vol. 29, no. 5, pp. 1151–1158, Sep. 2010.

[14] M. A. Arjona, M. Cisneros-Gonzalez, and C. Hernandez, "Parameter estimation of a synchronous generator using a sine cardinal perturbation and mixed Stochastic–Deterministic algorithms," *IEEE Trans. Ind. Electron.*, vol. 58, no. 2, pp. 486–493, Feb. 2011.

[15] M. Cisneros-González, C. Hernandez, R. Morales-Caporal, E. Bonilla-Huerta, and M. A. Arjona, "Parameter estimation of a synchronous-generator two-axis model based on the standstill chirp test," *IEEE Trans. Energy Convers.*, vol. 28, no. 1, pp. 44–51, Mar. 2013.

[16] A. M. A. Oteafy, J. N. Chiasson, and S. Ahmed-Zaid, "Development and application of a standstill parameter identification technique for the synchronous generator," *Int. J. Electr. Power Energy Syst.*, vol. 81, pp. 222–231, Oct. 2016.

[17] T. Kano, Y. Watanabe, T. Ara, and T. Matsumura, "Calculation of equivalent circuit constants of synchronous machines considering field transient characteristics using DC decay testing method with open and shorted field windings," *Electr. Eng. Jpn.*, vol. 178, no. 2, pp. 39–46, Jan. 2012.

[18] F. Maurer, M. T. Xuan, and J.-J. Simond, "Two full parameter identification methods for synchronous machine applying DC-decay tests for a rotor in arbitrary position," *IEEE Trans. Ind. Appl.*, vol. 53, no. 4, pp. 3505–3518, Jul. 2017.

[19] F. K. Dalton and A. W. W. Cameron, "Simplified measurement of sub-transient and negative sequence reactances in salient-pole synchronous machines [includes discussion]," *Trans. Amer. Inst. Electr. Eng. III, Power App. Syst.*, vol. 71, no. 4, pp. 752–757, Oct. 1952.

[20] I. M. Canay, "Modelling of alternating-current machines having multiple rotor circuits," *IEEE Trans. Energy Convers.*, vol. 8, no. 2, pp. 280–296, Jun. 1993.

[21] I. M. Canay, "Determination of model parameters of synchronous machines," *IEE Proc. B, Electr. Power Appl.*, vol. 130, no. 2, pp. 86–94, Mar. 1983.

[22] H. Liu, W. Wang, C. Xiang, L. Han, and H. Nie, "A de-noising method using the improved wavelet threshold function based on noise variance estimation," *Mech. Syst. Signal Process.*, vol. 99, pp. 30–46, Jan. 2018.

YIMING MA received the B.Eng. degree in electrical engineering from the Huazhong University of Science and Technology (HUST), China, in 2013, where he is currently pursuing the Ph.D. degree with the School of Electrical and Electronic Engineering.

His research interests include dynamic analysis and parameter estimation of large synchronous machine and multi-objective surrogate-assisted design optimization of permanent magnet machines.

LIBING ZHOU received the B.S., M.S., and Ph.D. degrees in electrical engineering from the Huazhong University of Science and Technology (HUST), China, in 1982, 1985, and 1993, respectively.

He is currently a Professor with HUST. His research interests include electromagnetic design, operation analysis, and drives of AC machines.

JIN WANG (Member, IEEE) received the B.S., M.S., and Ph.D. degrees in electrical engineering from the Huazhong University of Science and Technology (HUST), China, in 2002, 2005, and 2010, respectively.

From 2010 to 2013, he was a Postdoctoral Fellow with HUST. He is currently an Associate Professor with HUST. His research interests include electro-magnetic design and analysis of permanent magnet machines and superconducting generators.